Regional modelling of Saharan dust and biomass-burning smoke

Part I: Model description and evaluation

By BERND HEINOLD[1,2]*, INA TEGEN[1], KERSTIN SCHEPANSKI[2], MATTHIAS TESCHE[1], MICHAEL ESSELBORN[3,4], VOLKER FREUDENTHALER[5], SILKE GROSS [5], KONRAD KANDLER[6], PETER KNIPPERTZ[2], DETLEF MÜLLER[1,7], ALEXANDER SCHLADITZ[1], CARLOS TOLEDANO[5], BERNADETT WEINZIERL[3], ALBERT ANSMANN[1], DIETRICH ALTHAUSEN[1], THOMAS MÜLLER[1], ANDREAS PETZOLD[3] and ALFRED WIEDENSOHLER[1], [1]*Leibniz Institute for Tropospheric Research, 04318 Leipzig, Germany;* [2]*School of Earth and Environment, University of Leeds, Leeds LS2 9JT, UK;* [3]*Deutsches Zentrum für Luft- und Raumfahrt, Institut für Physik der Atmosphäre, 82234 Oberpfaffenhofen, Germany;* [4]*European Southern Observatory (ESO), 85748 Garching, Germany;* [5]*Meteorological Institute, Ludwig-Maximilians-Universität, 80333 Munich, Germany;* [6]*Institute of Applied Geosciences, Darmstadt University of Technology, 64287 Darmstadt, Germany;* [7]*Atmospheric Remote Sensing Laboratory, Gwangju Institute of Science and Technology, Buk-Gu Gwangju 500-712, Republic of Korea*

ABSTRACT

The spatio-temporal evolution of the Saharan dust and biomass-burning plume during the SAMUM-2 field campaign in January and February 2008 is simulated at 28 km horizontal resolution with the regional model-system COSMO-MUSCAT. The model performance is thoroughly tested using routine ground-based and space-borne remote sensing and local field measurements. Good agreement with the observations is found in many cases regarding transport patterns, aerosol optical thicknesses and the ratio of dust to smoke aerosol. The model also captures major features of the complex aerosol layering. Nevertheless, discrepancies in the modelled aerosol distribution occur, which are analysed in detail. The dry synoptic dynamics controlling dust uplift and transport during the dry season are well described by the model, but surface wind peaks associated with the breakdown of nocturnal low-level jets are not always reproduced. Thus, a strong dust outbreak is underestimated. While dust emission modelling is a priori more challenging, since strength and placement of dust sources depend on on-line computed winds, considerable inaccuracies also arise in observation-based estimates of biomass-burning emissions. They are caused by cloud and spatial errors of satellite fire products and uncertainties in fire emission parameters, and can lead to unrealistic model results of smoke transport.

1. Introduction

The African continent contains the World's most important sources of desert dust and biomass-burning aerosol, which each represent a major component of the atmospheric aerosol load. The Sahara desert and the Sahelian region contribute at least 50% to the global dust emissions (Washington et al., 2003) and a con-siderable amount of smoke particles originates from biomass-burning activities in southern West Africa that are mainly caused by grassland and savanna fires (e.g. Barbosa et al., 1999; Andreae and Merlet, 2001; van der Werf et al., 2006, 2010). Saharan dust and vegetation-fire smoke are transported across the tropical Atlantic Ocean. During the peak season for land fires in boreal winter, Saharan dust layers merge with West African fire plumes resulting in a complex aerosol layering (Haywood et al., 2008). Desert dust and biomass-burning parti-cles affect the global and regional energy balance by changing at-mospheric heating rates, temperatures and stability as well as the

hydrological cycle (e.g. Sokolik and Toon, 1996; Myhre et al., 2003; Miller et al., 2004; Yoshioka et al., 2007; Myhre et al., 2008; Solmon et al., 2008). Still, considerable uncertainties remain in particular with regard to magnitude and sign of the radiative effects. This is due to uncertainties in the quantification of the highly variable distribution and complex vertical layer structure and optical properties of dust and smoke aerosol (IPCC, 2007).

The first field campaign of the SAharan Mineral dUst experiMent (SAMUM-1; Heintzenberg, 2009) was carried out in Morocco in May and June 2006. This column closure experiment for desert dust aimed at quantifying the optical properties and the direct radiative forcing of Saharan dust near source regions. During SAMUM-1 a regional model system was developed for simulations of Saharan dust emissions, transport and radiative effects (Heinold et al., 2008, 2009; Laurent et al., 2010; Tegen et al., 2010). Compared to global models of the dust cycle, regional modelling allows to compute surface properties and transport processes at scales that are small enough to resolve more of the meteorological processes controlling dust processes (Zender et al., 2003). The second field experiment (SAMUM-2) that was carried out on Cape Verde in January and February 2008 focused on the characterization of the mixed plume of Saharan dust and biomass-burning aerosol transported off the West African continent. A unique data set of remote sensing measurements and in situ particle analysis is available for investigations on the complex aerosol layering including radiative effects and aging processes on mineral dust particles during long-range transport (Ansmann et al., 2011). Within SAMUM-2, the regional model is used to simulate the spatio-temporal evolution of the mixed plume of Saharan dust and biomass-burning aerosol. For this purpose, model parametrizations including, for example, the wet deposition parametrization and the prescription of preferential dust sources, were improved. In addition, a scheme for vegetation-fire emissions of smoke particles was developed. The results of this regional dust and smoke model provide a spatio-temporal context to the experimental data collected during the SAMUM-2 field campaign. They also provide essential input for follow-up studies on the aerosol radiative effect on regional synoptic parameters presented by Heinold et al. (2011). In turn, the regional model system can be evaluated on the basis of many different and independent measurements in order to test the validity of model parametrizations.

Here we make use of the comprehensive set of observational data taken during the SAMUM-2 field campaign for a detailed model evaluation. The comparisons with field measurements and satellite retrievals will show whether the model is capable of reproducing the emission and transport of Saharan dust and biomass-burning particles. Particular attention is on the complex vertical structure of aerosol layers over the tropical Atlantic Ocean. Its good representation by the model is considered as pre-requisite for further investigations on radiative effects and feedbacks on meteorology.

2. Model description and methods

2.1. Regional model COSMO-MUSCAT

The distribution of Saharan dust and biomass-burning aerosol is simulated using the regional model system COSMO-MUSCAT. It is based on the dust model that was developed within the first phase of SAMUM (Tegen et al., 2006; Heinold et al., 2007, 2009). The parallelized multiscale regional model system consists of the non-hydrostatic model COSMO (formerly named Lokal-Modell, LM) (Steppeler et al., 2003) as meteorological driver, and the online-coupled 3-D chemistry tracer transport model MUltiScale Chemistry Aerosol Transport Model (MUSCAT) (Wolke et al., 2004; Renner and Wolke, 2010). In MUSCAT, microphysical processes and chemical reactions are described by time-dependent mass balance equations. The advection of chemical species and aerosols is computed by a third-order upstream scheme; an implicit–explicit scheme is applied for temporal integration (Knoth and Wolke, 1998; Wolke and Knoth, 2000). Emission, transport and deposition of aerosol particles are simulated using meteorological and hydrological fields from COSMO updated every advection time step (here, two COSMO time steps of 45 s). The model accounts for subgridscale convective mass fluxes according to Tiedtke (1989). The removal of aerosol particles from atmosphere is due to dry and wet deposition processes. The computation of dry deposition follows Seinfeld and Pandis (1998) and Zhang et al. (2001). Wet deposition, that is, rain-out and wash-out, is parametrized following Berge (1997) and Jakobson et al. (1997). The deposition rates are given by

$$\Delta c_{\text{rain–out}} = -c_{\text{dust, smoke}}(j, k) \frac{W_{\text{in}}(j) \cdot P}{\Delta z(k) \cdot \rho_w} \tag{1}$$

and

$$\Delta c_{\text{wash–out}} = -c_{\text{dust, smoke}}(j, k) E(j) \frac{A \cdot P}{v_{dr}}, \tag{2}$$

where $c_{\text{dust, smoke}}(j, k)$ is the particle concentration of size bin j at the vertical level k, $\Delta z(k)$ is the increment of each vertical level k and $W_{in}(j)$ is the rain-out scavenging ratio. ρ_w is the water density, P the precipitation rate and E the size-dependent collection efficiency by raindrops. $A = 5.2$ m^3 kg^{-1} s^{-1} denotes an empirical coefficient (assuming the Marshall–Palmer precipitation size distribution) and $v_{dr} = 5$ m s^{-1} the raindrop settling velocity. The details of the parametrization are taken from Tsyro and Erdman (2000) and are applied to each dust bin and biomass-burning particles. In order to consider the enhanced aerosol particle removal by convective precipitation, in particular close to the Inter Tropical Convergence Zone (ITCZ), the wet deposition scheme has been adapted by increasing the subcloud scavenging efficiency E to 1.0 in the case of moist convection. To compensate for potential biases in simulating precipitation over the tropical Atlantic Ocean, the modelled rain rates are adjusted to the daily global-gridded 0.25° × 0.25° Tropical Rainfall

Measuring Mission (TRMM) 3B42 V6 product (Simpson et al., 1996), when precipitation events south of 20°N are missed or underestimated. The correction is only applied in MUSCAT and does not affect the COSMO meteorology.

The COSMO-MUSCAT simulations include an online feedback of the computed dust and smoke aerosol on the solar and terrestrial radiation fluxes and on the atmospheric dynamics in the meteorological model. The dust optical properties in this study are computed from Mie theory using the refractive indices from laboratory measurements reported by Sokolik and Toon (1999). We assume an internal mixture of 98% kaolinite and 2% hematite resulting in a single scattering albedo of, for example, 0.79 at 250–700 nm and 0.98 at 700–1530 nm for dust particles of 1.5 μm effective radius (Helmert et al., 2007). Highly absorptive optical properties are prescribed for biomass-burning particles, which are characteristic for freshly emitted smoke particles from intense African savanna and grass fires (Reid et al., 2005b). Accordingly, the single scattering albedo of smoke particles is 0.52 and 0.45 for the 250–700 nm and 700–1530 nm wavelength band, respectively. As another important controlling parameter for radiative forcing, the surface albedo retrieval from MODIS (Moody et al., 2005) is used instead of the standard surface albedo in the COSMO model. For a more detailed description on optical properties, radiative effects and atmospheric dynamic feedbacks of mineral dust and biomass-burning particles, we refer to Heinold et al. (2011).

2.2. Dust emission scheme

Dust emissions in sparsely or non-vegetated areas depend on surface wind friction velocities, surface roughness, soil texture and soil moisture. Based on COSMO first-layer winds (about 34 m above ground level, agl) and soil moisture, dust emissions are calculated using the emission scheme by Tegen et al. (2002). The emission fluxes F (in g m^{-2} s^{-1}) are given by

$$
F = \alpha \frac{\rho_a}{g} u_*^3 \sum_i \left[\left(1 + \frac{u_{*t}(D_{p_i})}{u_*} \right) \left(1 - \frac{u_{*t}^2(D_{p_i})}{u_*^2} \right) \Delta s_i \right] \\
\times A_{\text{eff}} \left(1 - A_{\text{snow}} \right) I_\Theta ,
$$

(3)

where α is the sandblasting efficiency, ρ_a denotes the air density, g is the gravitational constant and u_* is the surface friction velocity. u_{*t} is the threshold friction velocity depending on the soil particle diameter D_{p_i} of size fraction i. These size classes are assumed to be lognormally distributed with mode diameters between 2 μm and 710 μm. The relative surface area covered by a size fraction is represented by s_i, I_Θ is the influence of soil moisture, A_{eff} is the erodible area depending on the seasonal variations in vegetation cover and A_{snow} is the part of A_{eff} covered by snow. The threshold friction velocities for initial dust mobilization are computed as function of soil particle size distribution following Marticorena and Bergametti (1995). COSMO first-layer winds and high-resolved roughness lengths from remote

sensing for northern Africa (Laurent et al., 2008) serve to calculate the wind friction velocities assuming neutral atmospheric stratification. Compared to the earlier model version (Heinold et al., 2009), the location and extent of preferential dust sources are now prescribed on the basis of Meteosat Second Generation (MSG) satellite observations. Dust emission is computed only at those grid cells where source activation was observed at least two times during the years 2006–2009 in the maps of dust source activations (DSAs), which were derived from MSG infrared dust index images by Schepanski et al. (2007) including updates. Emissions of Bodélé dust are described according to Tegen et al. (2006) considering the specific characteristics of diatomite sediment, which is the dominant soil constituent in this region. The modelled dust is transported as passive tracer in five independent size classes within the diameter range 0.2–48 μm.

2.3. Vegetation-fire emission scheme

The emission of trace gases and aerosol particles (in mol day^{-1} and g day^{-1}, respectively) that originate from biomass burning are computed for individual fire pixels as a product of the daily burnt area $A_{\text{burn}, k}$, the burning efficiency BE_k, the empirical emission factor $EF_{X, k}$ and the available fuel load or biomass density $M_{\text{biomass}, k}$ following the basic approach of, for example, Seiler and Crutzen (1980):

$$
M_X = \sum_k [M_{\text{biomass}, k} \cdot A_{\text{burn}, k} \cdot EF_{X, k} \cdot BE_k].
$$

(4)

The subscripts X and k indicate the dependency on the emitted species and the biome of the fire site, respectively. In order to characterize the location and the temporal variability of fires, the Moderate-Resolution Imaging Spectroradiometer (MODIS) fire detection products: (1) burned area maps at 500 m and (2) daily active fire counts at 1 km resolution (Justice et al., 2002; https://lpdaac.usgs.gov) are used. The MODIS sensors are operated on board the sun-synchronous polar-orbiting satellites Terra and Aqua and collect observations of almost the entire Earth four times a day at around 10:30 and 22:30 (Terra) and 01:30 and 13:30 (Aqua), equatorial local time. The burning efficiencies for main vegetation types are taken from Reid et al. (2005a), and the species-depended emission factors are based on Andreae and Merlet (2001) including several updates. Although the compilation of emission factors comprises more than 100 species, here the focus is on particles of diameter smaller than 2.5 μm (PM2.5) (see Table 1). The mean volume particle diameter is 0.5 μm including aerosol ageing and hygroscopic growth. Due to continuously high humidity within the smoke layer a constant hygroscopic growth factor of 1.35 (Reid et al., 2005b) is assumed. A map of biomass density is generated by combining two different data sets. For the woody vegetation in tropical Africa we make use of a digital database containing maximum potential above-ground biomass,

Table 1. Emission parameters of biomass-burning aerosol (PM2.5) used in COSMO-MUSCAT

	Biome	Emission factor[a] EF (g kg^{-1})	Burning efficiency[b] BE
1	Evergreen needleleaf forest	13.0	0.5
2	Evergreen broadleaf forest	9.1	0.5
3	Deciduous needleleaf forest	13.0	0.5
4	Deciduous broadleaf forest	9.1	0.5
5	Mixed forests	9.1	0.5
6	Closed shrublands	4.9	0.6
7	Open shrublands	4.9	0.6
8	Woody savannas	4.9	0.6
9	Savannas	4.9	0.85
10	Grasslands	4.9	0.85
11	Permanent wetlands	4.9	0.5
12	Croplands	3.9	0.85
13	Urban and built-up	—	—
14	Cropland mosaics	4.9	0.6
15	Snow and ice	—	—
16	Barren/sparsely vegetated	4.9	0.85
17	Water bodies	—	—

Notes: The values represent averages over large numbers of fires taken from compilations by Andreae and Merlet (2001) and Reid et al. (2005a). For simplification, the parameters do not account for different phases of combustion (i.e. flaming and smouldering), even though this assumption is not verified. The ecosystem assignment in Andreae and Merlet (2001) and Reid et al. (2005a) is adapted to the IGBP classes in MODIS land-cover data, which is used in the vegetation-fire scheme.
[a]From Andreae and Merlet (2001) including several updates.
[b]From Reid et al. (2005a).

which is provided by the Carbon Dioxide Information Analysis Center (CDIAC; http://cdiac.esd.ornl.gov) for the years 1980 and 2000 (Brown and Gaston, 1996; Gibbs et al., 2007). The annual net primary productivity (NPP) at 1 km spatial resolution derived from MODIS/Terra measurements (Running et al., 2000; Thornton et al., 2002; available at http://ntsg.umt.edu) serves as an approximation for the available biomass in savannas and grasslands. The distinction between vegetation types is based on the MODIS land cover product providing an International Geosphere-Biosphere Programme (IGBP) vegetation classification map (Friedl et al., 2002; https://lpdaac.usgs.gov).

Besides deep tropical clouds that hamper the detection of fires by satellite, baseline uncertainties in modelled biomass-burning emissions result from the spatial error in satellite fire location data (i.e. the assignment of fire pixels to the correct vegetation type). Hyer and Reid (2009) estimate that vegetation-fire emissions based on MODIS fire data have a positive bias of 3–19%. The estimate is made for biomass burning in the Amazon basin, but might be valid also for West African sources, as the problem is of geometric nature. Other emission model parameters are

associated with even larger errors, for example, the uncertainty of 50–100% in the potentially available biomass shown by Reid et al. (2005a). A particular problem are the patterns of fire activities in MODIS data, which vary systematically on even and odd days. They result from the geographical coverage of the satellite sensors [overpass time: 10:30 and 22:30 (Terra), 01:30 and 13:30 (Aqua), equatorial local time] and are likely related to the different cloud-cover conditions. Gaps in active fire maps alternately affect Nigeria and Cameroon or Ghana, Togo and Benin. Here, the discontinuities are filled with fire information of the previous day in order to obtain temporally continuous data, although this distorts the day-to-day variations in some regions.

Figure 1 illustrates the spatial distribution of land-use patterns, biomass density and the area burned during January 2008 in West Africa. The emission scheme provides daily point source emissions on an auxiliary grid of $0.1° \times 0.1°$ spatial resolution. The typical diurnal cycle of fire activities is approximated by weighting the emissions by a factor of 1.25 for daytime hours (07:00–18:00 UTC) and 0.75 otherwise. Within West African emission areas, smoke particles are effectively lifted from surface by convective transport. Due to atmospheric conditions of high instability related to the ITCZ, deep convection over the sun-heated ground is more efficient in vertical mixing than the buoyancy effect of fire plumes (Haywood et al., 2008). While moist convective aerosol transport is parametrized in MUSCAT, small-scale convection initiated by fires is not yet considered by the model. As approximation, smoke particles are released at different injection heights: 20% below 100 m, 30% between 100 m and 500 m and 50% from 500 m to 1500 m. The vertical range of injection heights is originally used for simulations of Eastern European vegetation-fires with the Fire Assimilation System (FAS) of the Finnish Meteorological Institute (FMI, Sofiev et al., 2009). In a sensitivity study, we found that the injection heights are also suitable to describe the uplift of West African fire products.

2.4. Model setup

The regional dust and vegetation-fire simulations for the SAMUM-2 field campaign are performed with 28 km horizontal grid spacing and 40 vertical layers, with the lowest layer reaching 68 m above ground. The model domain spans from the southwest corner at 0.2°N, 32.3°W to the northeast corner at 41.1°N, 32.9°E and covers relevant Saharan dust sources, West African vegetation-fires and the eastern Tropical Atlantic Ocean including the SAMUM-2 field site at Praia/Santiago, Cap Verde (14.9°N, 23.5°W). The model was run for almost the entire period of SAMUM-2 from 10 January to 7 February 2008. For model evaluation, particular focus is on the days of 25, 28 and 31 January as well as 6 February 2008, for which data of many colocated airborne and ground-based measurements are available. Six-hourly updated analysis fields from the
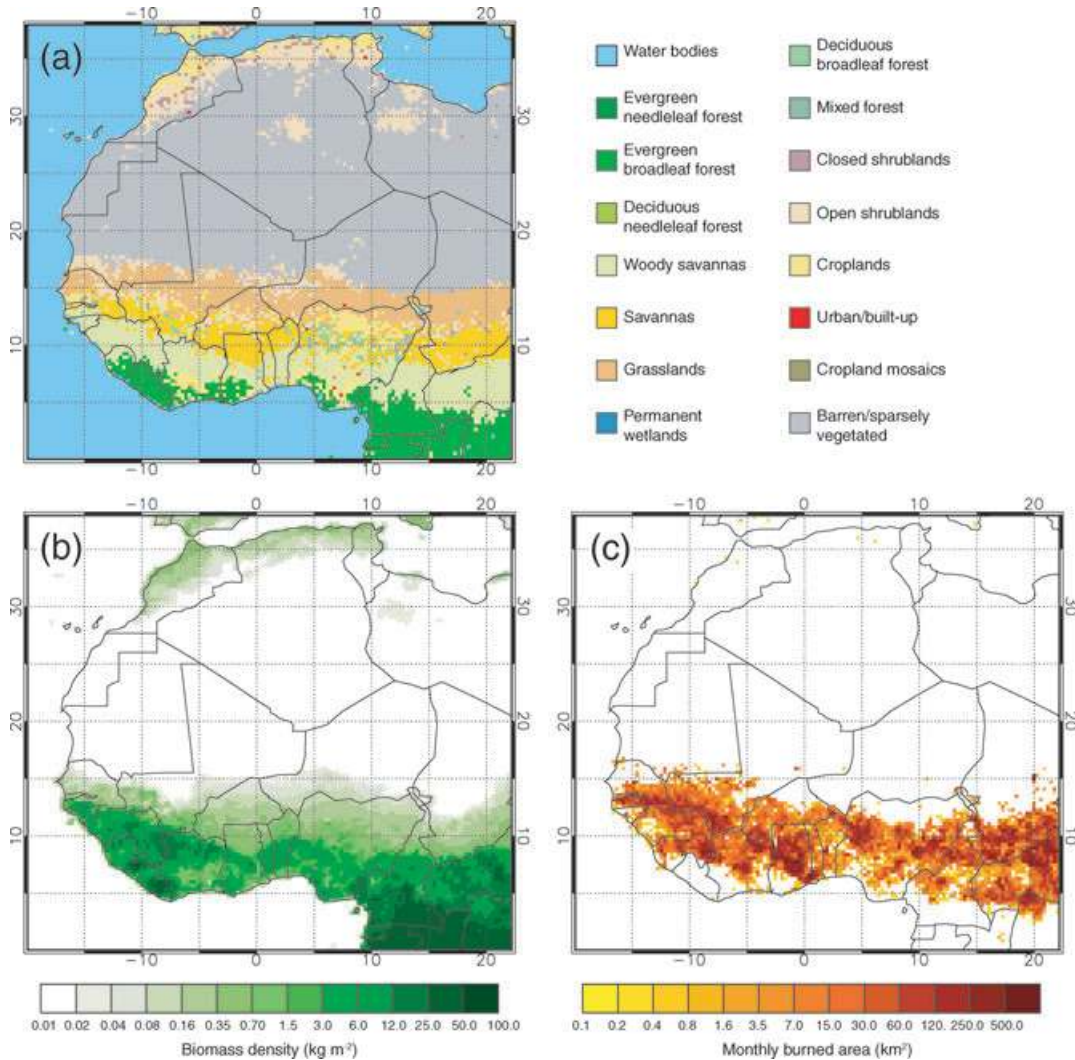
Fig. 1. Maps of West Africa showing (a) land-use patterns from MODIS and (b) biomass density, which is compiled from a database of maximum potential aboveground biomass of woody vegetation provided by CDIAC and the MODIS annual net primary productivity (NPP) for savannas and grasslands. (c) Map of burned area detected by MODIS in January 2008.

German weather service (Deutscher Wetterdienst, DWD) global model GME (Majewski et al., 2002) provide initial and lateral boundary conditions to drive COSMO-MUSCAT. The model runs are reinitialized every 48 h to keep the meteorology close to the analysis fields. After 24 h spin-up time for the COSMO model, MUSCAT is coupled to compute the aerosol transport processes. The first cycle starts with zero aerosol concentrations, following cycles are initialized using the aerosol load from the previous run. For model evaluation, aerosol optical thicknesses (AOTs) at 550 nm are computed from the simulated dust distributions as

$$\tau = \frac{3}{4} \sum_j \frac{Q_{ext, 550 nm}(r_{eff}(j))}{r_{eff}(j)\,\rho_{dust}} M(j),\qquad(5)$$

where $Q_{ext, 550 nm}(j)$ is the dust extinction efficiency at 550 nm depending on the effective radius $r_{eff}(j)$ of the particle size class j. ρ_{dust} is the particle density (2650 kg m^{-3}) and $M(j)$ is the column mass load of mineral dust. The values of $Q_{ext, 550 nm}$ are calculated from refractive indices from Sokolik and Toon (1996) and are 1.684, 3.165, 2.352, 2.145 and 2.071 for the five size fractions, respectively. Smoke optical thicknesses are calculated as a product of the mass extinction coefficient at the corresponding wavelengths, for example, 4.5 m^2 g^{-1} at 550 nm (Reid et al., 2005b) (plus hygroscopic growth), and the mass load of biomass-burning aerosol. In addition, profiles of particle extinction and backscatter coefficients at 355 and 532 nm are derived from the model results. For the conversion, an extinction-to-backscatter ratio (lidar ratio) of 55 sr and 70 sr is used for

mineral dust and for smoke aerosol, respectively (Tesche et al., 2009).

2.5. Measurements during SAMUM-2

The SAMUM-2 field campaign took place in the Cape Verdes from 15 January to 14 February 2008. Numerous in situ and remote sensing observations were collected at the airport of Praia, Cape Verde. Measurements taken aboard the research aircraft Falcon complement the ground-based measurements characterizing the mixed plume of Saharan dust and biomass-burning particles. In this study we make use of (1) the particle AOT measured at Praia with an Aerosol Robotic Network (AERONET; Holben et al., 1998; Toledano et al., 2011) sun photometer (CIMEL Electronique 318A spectral radiometer), which measures sun and sky radiances at seven wavelengths (340–1640 nm). Here, only AOTs at 440 nm are considered. (2) Profiles of the 532-nm backscatter coefficient from the six-wavelength Backscatter Extinction lidar-Ratio Temperature Humidity profiling Apparatus (BERTHA) of the Leibniz Institute for Tropospheric Research (IfT) (Althausen et al., 2000; Tesche et al., 2009; 2011) are used to validate the vertical profiles of the modelled dust and smoke plume over Praia. The lidar data have a spatial and temporal resolution of 15 m and 10 s, respectively. As described by Tesche et al. (2009), dust and smoke backscatter profiles are separated and can be compared independently. Measurements of the extinction coefficient at 355 nm from the portable lidar system (POLIS) of the Meteorological Institute of the University Munich (MIM) (Heese et al., 2002; Gross et al., 2011) are also used for model evaluation. The POLIS overlap of only 70 m allows for trustworthy extinction profiles below 1 km height. (3) The model-derived dust size distribution is compared with near-surface particle number size distributions for particles with diameters between 20 nm and 20 μm measured at Praia. The particle diameter size range of 20 nm $\leq D \leq 10\,\mu$m was measured quasi-continuously by the combination of a Differential Mobility Particle Sizer (DMPS) and an Aerodynamic Particle Sizer (APS). Particles with $4 \leq D \leq 500\,\mu$m were measured by impactor collection on coated glass substrates once a day (Kandler et al., 2011a,b; Schladitz et al., 2011). However, the measurements are truncated at 20 μm when compared with the modelled dust particle size to exclude locally emitted large particles (Kandler et al., 2011b). (4) Several flight experiments were conducted to measure the vertical distribution of dust and smoke particles above the observation site. The Falcon aircraft of the German Aerospace Center (DLR) carried the airborne nadir-looking High Spectral Resolution Lidar (HSRL) providing vertical slices of extinction and backscatter coefficients at 532 nm (Esselborn et al., 2009), which are compared to the model-derived dust and smoke extinction coefficients along the flight paths.

In addition, DSA maps derived from MSG satellite observations (Schepanski et al., 2007, 2009) and reports of World Meteorological Organisation (WMO) stations are used as qualitative indicator for dust mobilisation. The spatial and temporal distribution of modelled AOT of mineral dust and biomass-burning smoke is compared to satellite retrievals of the optical thickness by MODIS Aqua and the absorbing aerosol index (AI) from the Ozone Monitoring Instrument (OMI) (Levelt, 2002). The latter is qualitative indicator for the presence of absorbing aerosol including dust and smoke particles. The OMI AI data set is screened for clouds taking into account only grid cells where the reflectivity at 380 nm was <12%. A cloud screening is also applied to the model results. Grid points are excluded from the evaluation if the fractional cloud cover simulated by COSMO (Steppeler et al., 2003) exceeds 75%. For a quantitative validation, the model-derived AOTs of dust and biomass-burning aerosol are additionally compared with quality-assured and cloud-screened AOT data from three other AERONET stations: Izaña/Teneriffe (28.3°N; 16.5°W), Dakar (14.4°N; 17.0°W) and Cinzana (13.3°N; 5.9°W). The whole range of measurements used for model evaluation is summarized in Table 2.

3. Results

3.1. Sources of West African dust and smoke aerosol

3.1.1. Saharan dust emissions. The meteorological conditions that led to Saharan dust emissions during the SAMUM-2 field experiment are described in detail by Knippertz et al. (2011), who identified three main dust phases: 17–20 January, 24–26 January, and 28 January–2 February 2008. During all episodes a strong south–north pressure gradient prevailed over the Sahel and southern Sahara due to south-westward extensions of the Azores High. As a result, widespread and partly intense dust emissions occurred from the Mauritanian coast to the Bodélé Depression. Synoptic station reports and the MSG infrared dust index indicate that 60–75% of all dust mobilisation events were associated to the breakdown of nocturnal low-level jets (LLJs) generating peak surface winds that trigger dust uplift (Knippertz et al., 2011).

The location of dust emission areas is presented in a map of DSAs for the three dust phases in Fig. 2. Following Schepanski et al. (2007), dust emission events are detected in images of the MSG infrared dust index using a back-tracking approach. In maps with $1° \times 1°$ resolution, the first pixel, where dust uplift is observed, is recorded. Subsequent dust emission beneath the dust plumes cannot be clearly distinguished from transported dust. Accordingly, the DSA data is a low estimate of dust activity. In addition, reports of dust storms and dust raising from synoptic stations are depicted in Fig. 2. During the first two episodes, dust emissions were reported by several synoptic stations in Mauritania and Mali. While during this period the dust sources in this region are hard to detect on satellite images because of persistent high clouds (not shown), maps of the MSG dust

Table 2. List of local field measurements during the SAMUM-2 field campaign and standard aerosol observations that are used in this study to evaluate the modelled spatial-temporal distribution of Saharan dust and biomass-burning aerosol

Instrumentation/platform	Used property	Purpose in the evaluation
SAMUM-2 field measurements		
AERONET sun photometer (CIMEL CE-318A)	AOT at $\lambda = 440$ nm	Local temporal evolution of AOT
	Ångström exponent (380/500 nm)	Relative contribution of dust and smoke to the aerosol load
BERTHA lidar	Backscatter coefficient at $\lambda = 532$ nm, (separate for dust and smoke)	Local vertical structure of dust and smoke layers
POLIS lidar	Extinction coefficient at $\lambda = 355$ nm	Local vertical structure of dust and smoke layers
HSR-Lidar aboard Falcon aircraft	Vertical slices of extinction coefficients at $\lambda = 532$ nm	Vertical/horizontal distribution of dust and smoke aerosol
DMPS + APS/ Cascade impactor	Near-surface particle size distribution (20 nm $\leq D \leq$ 10 μm/ 4 μm $\leq D \leq$ 500 μm)	First-layer dust size distribution
Routine aerosol observations		
MODIS/Aqua satellite	AOT at $\lambda = 550$ nm	Horizontal dust/smoke distribution
OMI/Aura satellite	OMI AI	Horizontal dust/smoke distribution
SEVIRI/MSG satellite	Dust source activations (DSAs)	Dust mobilization
Synoptic station reports (WMO)	Dust reports	Dust mobilization
AERONET sun photometer at Cinzana, Dakar, Izaña	AOT at $\lambda = 440$ nm	Temporal evolution of AOT
	Ångström exponent (Dakar, Cinzana: 440/675 nm; Izaña: 380/500 nm)	Relative contribution of dust and smoke to the aerosol load

index show additional dust emissions in southwestern Algeria, northern Mali, Niger and in the Bodélé Depression. Note that the reporting weather stations are often downwind of the initial source areas shown in the DSA maps since sediment transport by wind plays an important role. The dust sources are well reproduced by the model (Figs 2d and e), except in northern Mali and southwest of the Hoggar mountains. In addition, dust emissions are modelled in northern Algeria and in Libya, some of which are confirmed by local station reports (Fig. 2).

An unusually persistent and intense high-pressure system with its centre over France controlled the weather conditions within dust phase 3. The associated south-north pressure gradient caused extensive dust emissions in a zonal belt from Mauritania to the Bodélé, with dust production being maximum on 26 and 27 January (Knippertz et al., 2011). In the model results, the location of dust uplift is mostly correctly placed (cf. Figs 2c and f). However, particularly on 26 January, the simulated dust emission rates in Mauritania and Mali are too low, and important dust sources in the border triangle Mali–Algeria–Niger are not activated by the model on 27 January. This leads to an underestimation of the dust transport across the Atlantic Ocean on 28 January as shown later in comparisons to OMI AI and

MODIS AOT. While the synoptic-scale meteorology and the LLJ formation are well matched by the model, the magnitude of the diurnal cycle in surface winds is underestimated in that case. The problem already addressed by Todd et al. (2008) and Schepanski et al. (2009) is illustrated in Fig. 3. Shown are the frequency of LLJ occurrence from 03:00 UTC to 09:00 UTC computed from COSMO-MUSCAT results for 26 January. Nocturnal LLJ conditions are assumed to prevail if the wind speed difference Δv between 925 hPa and 770 hPa exceeds an empirically threshold of 5 m s^{-1} (Schepanski et al., 2009). The model computes LLJs over the Sahel, South and West Sahara, the Bodélé Depression and central Algeria. Their positioning agrees with the MSG observations of DSAs between 03:00 UTC and 09:00 UTC on 26 January, which are attributed to the nocturnal LLJ phenomenon (contour lines in Fig. 3a). The diurnal distribution of near-surface (first-layer) wind speeds is investigated at three sample grid points (17.0°N, 2.8°W; 20.8°N, 2.8°W; 22.8°N, 2.9°W) and for the subdomain 15.0–22.0°N, 1.0–3.0°W in northern Mali, where dust emissions are often missed in the model simulations (Fig. 3b). On days with LLJ development, a sudden increase in wind speed is expected, when the nocturnal LLJ is mixed down to the surface after sunrise between 06:00
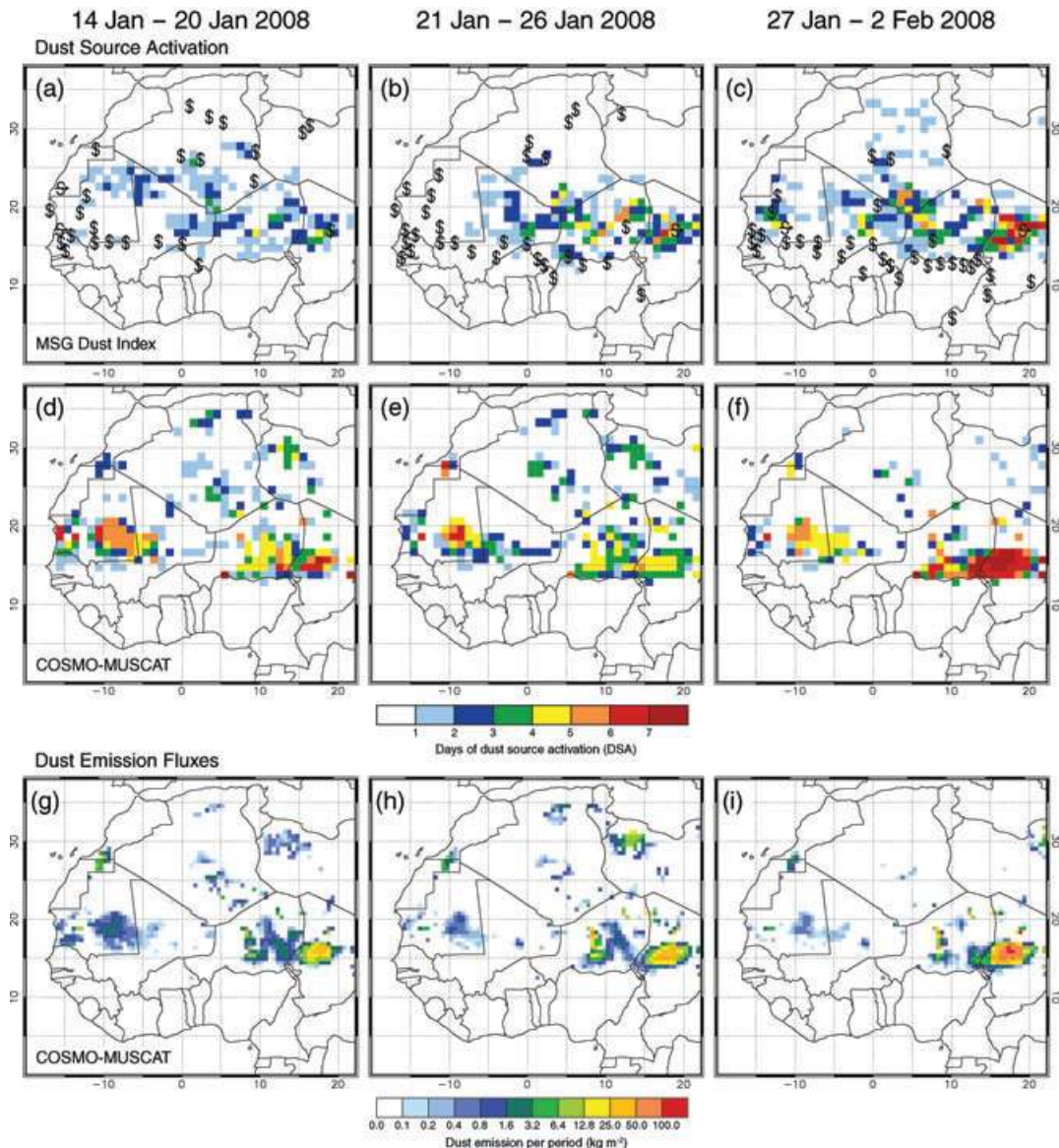
Fig. 2. Maps of dust emissions for three dust events during SAMUM-2 including up to 4 d prior the dust phases in Knippertz et al. (this issue) (DP1 14–20 January; DP2 21–26 January; DP3 27 January–2 February). (a–c) occurrence of dust emissions observed from MSG infrared difference images using a backtracking approach, overlaid with synoptic station reports of 'dust raised by the wind' ($) and 'dust storm' (→ S). (d–f) dust source activations and (h–i) emission fluxes computed with COSMO-MUSCAT.

and 15:00 UTC. The wind speed rapidly increases about 2 hours after sunrise at the northern grid point. Still, it takes 3 hours to reach the maximum of 7.5 m s^{-1}. An impulsive downward mixing of momentum is also not apparent for the other grid points and the mean. The modelled winds with maximum values between 5 and 7.5 m s^{-1} (Fig. 3b) are generally insufficient for dust uplift considering the gradient of wind velocity between the first model layer and surface. Time series of the vertical distribution of horizontal wind speed at two of the sample grid points in Figs 3c and d show that the vertical structure of the LLJ and its magnitude are very well represented. Vertically limited wind

speed maxima of up to 14 m s^{-1} are modelled between 0.5 and 1 km height in the night and morning. The breakdown of the nocturnal LLJ during the day is also evident in the wind profiles. However, the turbulent mixing takes places too gradually, which results in the missing peak surface wind speeds. The analysis suggests that shortcomings may exist in the planetary boundary layer scheme and/or the lower boundary conditions, i.e. model topography and surface roughness (Todd et al., 2008). Moreover, an underestimation of modelled surface winds and dust emission fluxes can occur in areas characterised by strong variations in small-scale topography that cannot be resolved explicitly.
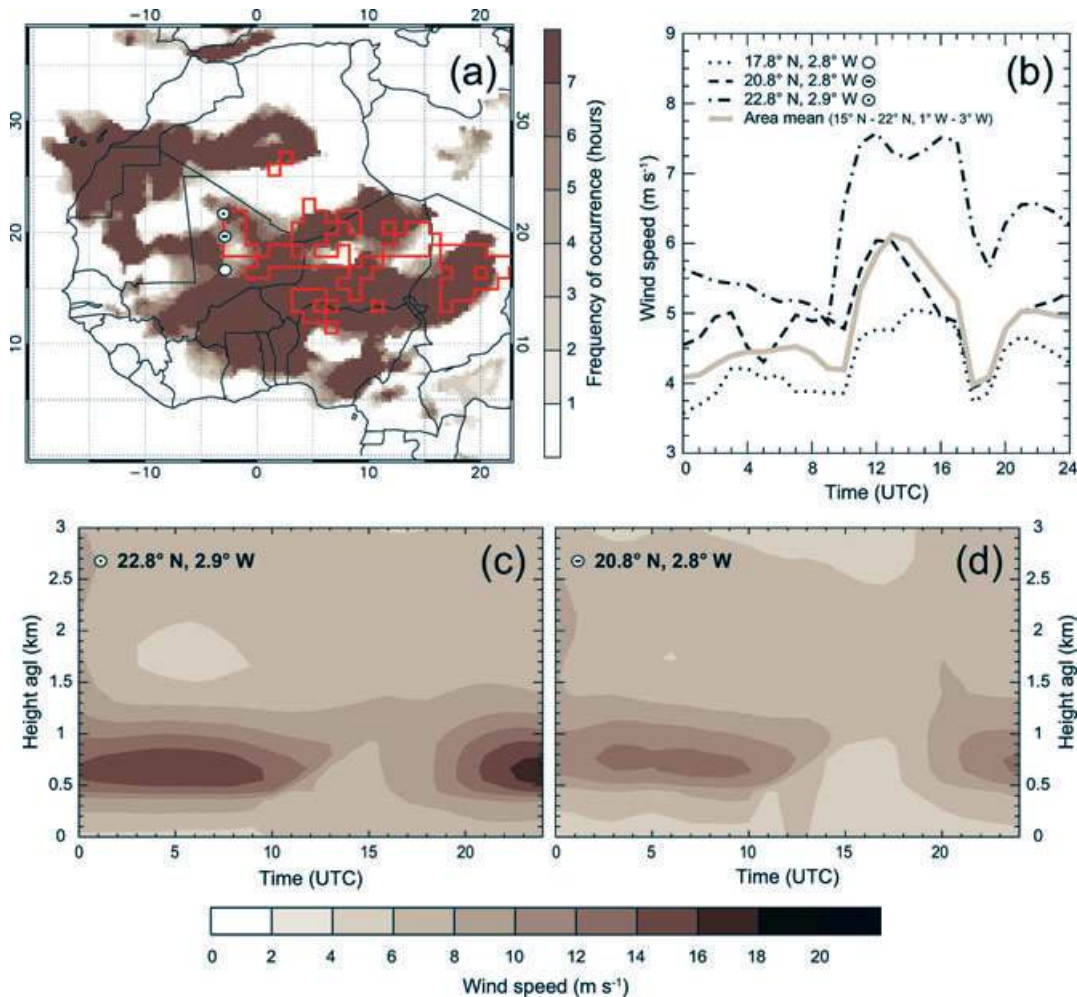
Fig. 3. Indicators for nocturnal LLJ formation and breakdown in COSMO-MUSCAT simulations on 26 January 2008. Map of (a) frequency of LLJ ($\Delta v \geq 5\,\mathrm{m\,s^{-1}}$ between levels at around 925 hPa and 770 hPa) occurrence from 03:00 UTC to 09:00 UTC in hours. The contour lines indicate MSG observations of DSA between 03:00 UTC and 09:00 UTC, which are assumed to be related to the nocturnal LLJ phenomenon. Time series of (b) COSMO first-layer wind speed for three sample grid points marked by circles in (a) and as mean over the domain 15.0–22.0°N, 1.0–3.0°W. Time series of (c, d) the vertical distribution of horizontal wind speed in $\mathrm{m\,s^{-1}}$ at two of the sample grid points.

This was shown in detail in an earlier study by Heinold et al. (2009).

For the remaining period, the dust model performs well in terms of spatio-temporal distribution and source strength of dust production. The total Saharan dust emissions simulated for the three dust phases of SAMUM-2 (14 January–2 February; Figs 2g–i) are 20 Tg. This value is reasonable when compared to results of previous studies. Estimates of mean dust emissions for the entire month of January range from 20 Tg to 31 Tg (D'Almeida, 1986; Laurent et al., 2008).

3.1.2. Biomass-burning aerosol emissions. The biomass-burning aerosol transported across the tropical Atlantic Ocean towards the Cape Verde Islands originates from a broad region of the African continent between latitudes 5°N and 11°N (Fig. 1c). The fire emissions, which are mainly anthropogenic and caused by agricultural burning, achieve their annual maximum during

the SAMUM-2 period. The majority of fire activities takes place in West African savannas (e.g. Barbosa et al., 1999; Fig. 1). Figure 4a shows a map of modelled PM2.5 emissions at 0.25° × 0.25° resolution averaged over the simulation period from 11 January to 7 February. Hot spot areas with point sources of more than 2.5 kg s^{-1} per grid cell are located in a band extending from Guinea to Ghana and in north-central Africa. The high amount of emitted smoke particles results from extensive burned areas and high available biomass density exceeding 5 kg m^{-2} in these regions. However, the highly productive sources are also characterised by long combustion times (cf. Figs 4a and b). On average, the fire grid cells are active on 8 days throughout the period of 28 days. The fires burn on average for 4.5 days continuously. There is a noticeable reduction of land fires to the end of the field campaign. The tendency is indicated by decreasing Ångström exponents observed at AERONET stations in the Sahel and
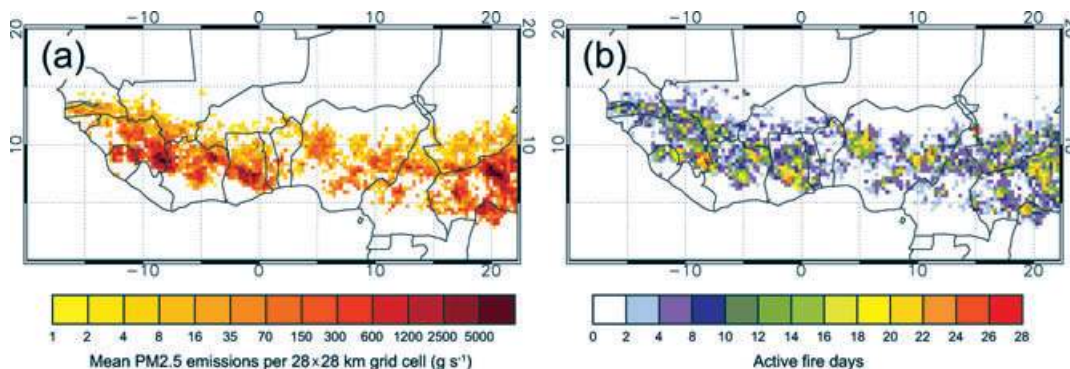
Fig. 4. Maps of (a) mean PM2.5 emissions in g s^{-1} and (b) number of active fire days at 0.25° × 0.25° resolution during the modelled period from 11 January to 7 February 2008.

sub-Sahel region of West Africa (see sun photometer observations at, e.g. Banizoumbou and Ilorin), while the AOT increases due to the seasonal enhancement of the dust cycle (Laurent et al., 2008). In fact, both the number of active fire pixels and the combustion time are reduced from 11 January to 7 February as shown in Fig. 5. As an exception, an increasing Ångström exponent is reported at the beginning of February for the sun photometer station Cinzana, where nearby land fires are observed during the entire period. The total biomass-burning emissions of PM2.5 accumulate to 2 Tg over the modelled time period.

3.2. Spatio-temporal evolution of dust and smoke transport

3.2.1. Horizontal distribution. During SAMUM-2 strong southward extensions of the Azores High across the western Mediterranean and northern Africa controlled the strength of the Harmattan winds transporting mineral dust from western Sahara to Cape Verde. To the south, synoptic-scale midlevel easterlies led to an efficient transport of biomass-burning aerosol from vegetation-fires over southern West Africa (Knippertz et al., 2011). The spatial and temporal evolution of dust and smoke transport is illustrated for the days 25, 28 and 31 January, and 6 February 2008 in Fig. 6. Shown are maps of model-derived optical thickness of dust/smoke and smoke aerosol at 550 nm, the MODIS/Aqua AOT and retrievals of OMI AI. Note that the MODIS AOT product is not sensitive to aerosol over bright desert surfaces, but can be used to detect biomass-burning smoke and mineral dust over vegetated areas and water surfaces. Blue areas in the maps of model-derived AOT and OMI AI indicate cloudiness that obscured the aerosol plume.

On 25 January, Saharan dust emissions reported by meteorological stations and indicated by OMI AI are not shown by the modelled AOT, apart from low dust loads over northern Mauritania, Niger and the Bodélé Depression. North of the Cape Verde Islands, the increase in AOT as observed by MODIS is not simulated, possibly since West African dust sources on previous days and the subsequent westward transport are
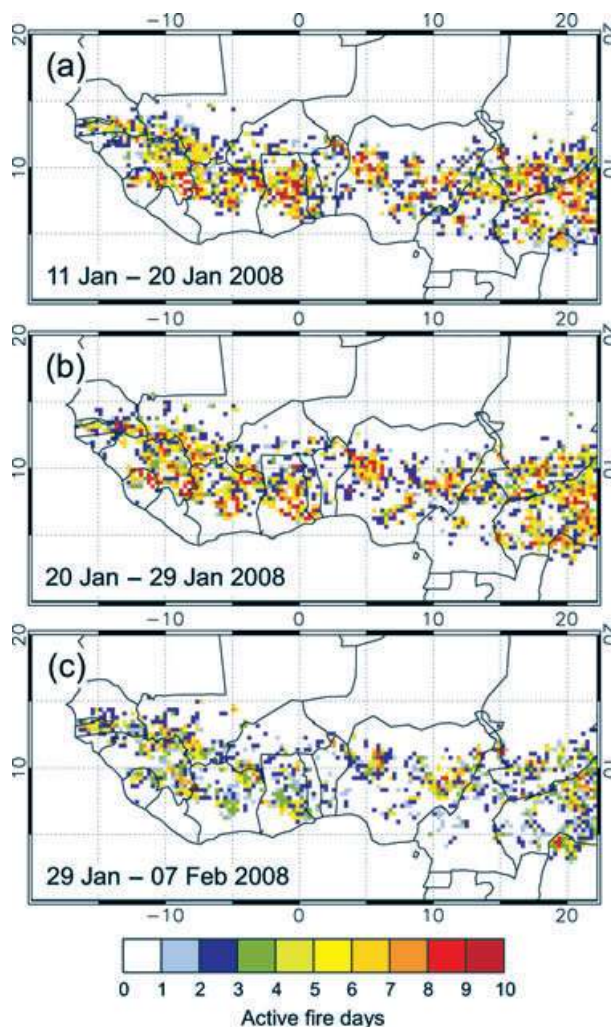

Fig. 5. Maps of number of active fire days at 0.25° × 0.25° resolution for 10-d periods: (a) 11–20 January, (b) 20–29 January and (c) 29 January–7 February 2008.
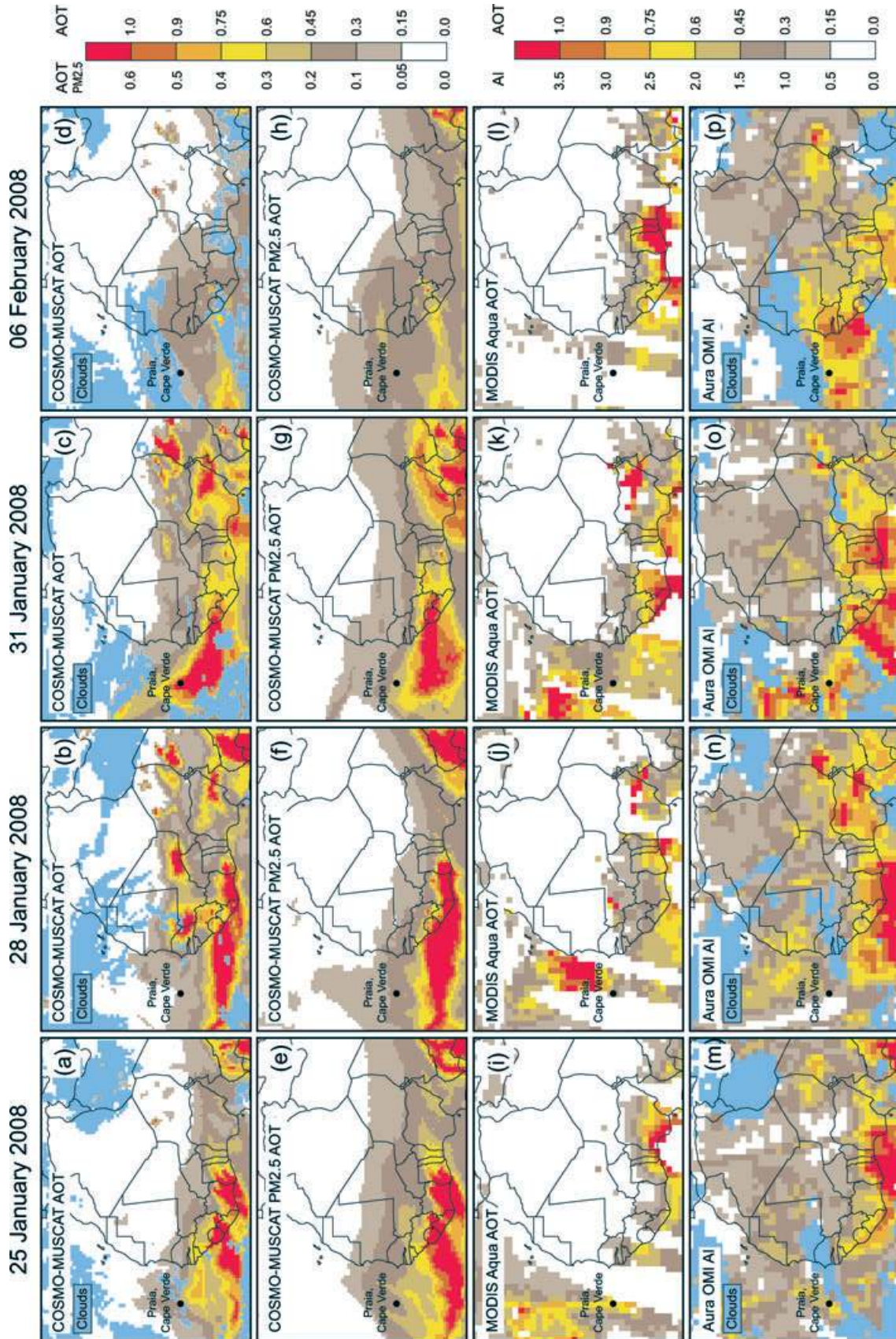
Fig. 6. Horizontal distribution of Saharan dust and biomass-burning aerosol on days: 25, 28 and 31 January and 6 February 2008. Shown are maps of model-derived aerosol optical thickness (550 nm) of (a–d) the dust/smoke plume and (e–h) only smoke aerosol, (i–l) MODIS Aqua optical thickness and (m–p) OMI aerosol index providing semiquantitative information on absorbing aerosol load. Note that the colour bar describes different units.

underestimated. However, the transport of the mixed plume from West Africa towards Cape Verde is well reproduced in the model results and the computed hot spots of biomass-burning aerosol over northern central Africa also agree well with MODIS and OMI AI observations. The smoke optical thickness appears to be overestimated over the West African coast. This overestimation of biomass-burning sources and the transport within possibly wrong tropospheric layers results in the unrealistic smoke transport towards the adjacent Gulf of Guinea and the open Atlantic Ocean (Figs 6a and m). In contrast, the persistent maximum aerosol load over the Bight of Benin is not reproduced by the model. It is unknown whether this is due to an underestimation of modelled smoke and Bodélé dust or an overestimation in the satellite retrievals, which are very sensitive to aerosol lifted to high altitudes by moist convective transport associated with the ITCZ. Another explanation might be the industrial and urban pollution from large urban settlements along the Gulf of Guinea coast that is not considered by the model but can contribute to the high amount of absorbing aerosol in this region.

A strong dust outbreak across the Atlantic Ocean occurred on 28 January. The model simulates several active dust sources in Mauritania and Mali as well as strong dust emissions in the Bodélé (Fig. 6b), which is in agreement with observations of OMI AI (Fig. 6n) and MSG-derived DSAs (Fig. 2c). In the model results, the dust transport towards the Atlantic is too weak, since the intense uplift of dust over northern Mauritania and Mali on 26 and 27 January driven by the breakdown of LLJs is underestimated (see Section 3.1.1). The advection of biomass-burning aerosol was directed westwards across the tropical Atlantic Ocean, so that the Cape Verde region was not affected by smoke. The transport patterns are well matched by the model, but the smoke optical thickness is overestimated when compared to MODIS measurements.

For 31 January, there is a good agreement of Saharan dust and smoke transport patterns between model simulations and satellite observations, although the fire emissions in Sierra Leone are too pronounced. As a consequence, the smoke-related AOT is overestimated over the tropical Atlantic Ocean south of the Cape Verde Islands. Northwest of the archipelago, MODIS and OMI AI retrievals show the plume of the dust outbreak on 28 January, which was transported westwards across the Atlantic Ocean. Due to the misrepresentation of this dust event the modelled dust optical thickness is too low in this region. However, the high dust load over northeastern Nigeria in the MODIS AOT map is well reproduced by COSMO-MUSCAT (cf. Figs 6c and k). The model also simulates a high amount of Bodélé dust and biomass-burning aerosol over the Bight of Benin in this case.

A period of nearly dust-free conditions at Praia site began on 6 February associated with the weakening of the subtropical high and only occasional, less widespread dust emissions in the Sahel (Knippertz et al., 2011). Lower dust emissions are simulated in comparison to previous days. The Bodélé Depression was still active, as confirmed by OMI AI. The satellite retrievals show smoke-dominated layers reaching Cape Verde from West African fires. In the model, the vegetation-fire activities are significantly reduced and the modelled transport path is more westwards than observed. Moreover, the high smoke concentration over an area extending from Cote d'Ivoire to Benin and the adjacent Gulf of Guinea is not matched by the simulations, even though this seems overestimated in the AOT map of MODIS compared to OMI AI observations.

In addition, the model is tested against sun photometer measurements of AOT at the locations Izaña, Praia, Dakar and Cinzana (Fig. 7). The Ångström exponent, which describes the spectral dependency of measured optical depth, is used as an indicator whether dust or smoke was dominant. It is close to zero for large dust particles, whereas values larger than one denote the presence of very small particles as in vegetation-fire smoke. Here, Ångström exponents larger than 0.3 define a smoke-dominated aerosol layer. Figure 7 shows the model-derived AOT due to biomass-burning particles and the total of dust and smoke aerosol. Grey shaded areas denote the days, on which the measured Ångström exponent was above the threshold of 0.3 and a high amount of biomass-burning aerosol most likely was present. The ratio of dust to vegetation-fire smoke as simulated by the model agrees in general very well with the temporal evolution of the measured Ångström exponents. Izaña located on Tenerife Island is remote from African biomass-burning emissions and only little affected by dust during boreal winter. The AOT remains mainly below 0.1, which is well reproduced by the model, except from an overestimation of the dust optical thickness between 27 and 30 January. For the SAMUM-2 field site Praia AOT values around 0.3 occurred at the beginning of the period and increased to 0.6–0.7 from 28 January to 3 February. The model underestimates both the dust and smoke optical thickness on 25 January. While the measurements reach up to 0.6, AOT values of only 0.4 are computed. Also the dust event on 28 January is misrepresented in the simulations for reasons already discussed earlier. However, a better agreement with respect to dust optical optical thickness is found on the following days. On 31 January, the modelled AOT is too high with a maximum of about 1.1. The overestimation is caused by the strong smoke transport towards the Cape Verdes (Fig. 6c) and an overpredicted dust load. At the stations Dakar and Cinzana, higher values of AOT than observed are computed by the model on days when the optical depth is underestimated at Praia. A significant overestimation is found at Cinzana on 27 and 28 January as well as two days later at Dakar. This indicates that the dust emission areas are not always correctly reproduced in the model. The model simulates too strong dust sources in western Mali (see Fig. 6c), which may also explain the overestimated AOT values at Praia on 31 January. Within the second part of the period, the modelled optical thicknesses show mostly a very good agreement with sun photometer measurements (Fig. 7). Only at Dakar an increase in AOT up to 0.75 on 6–7 February, which was most
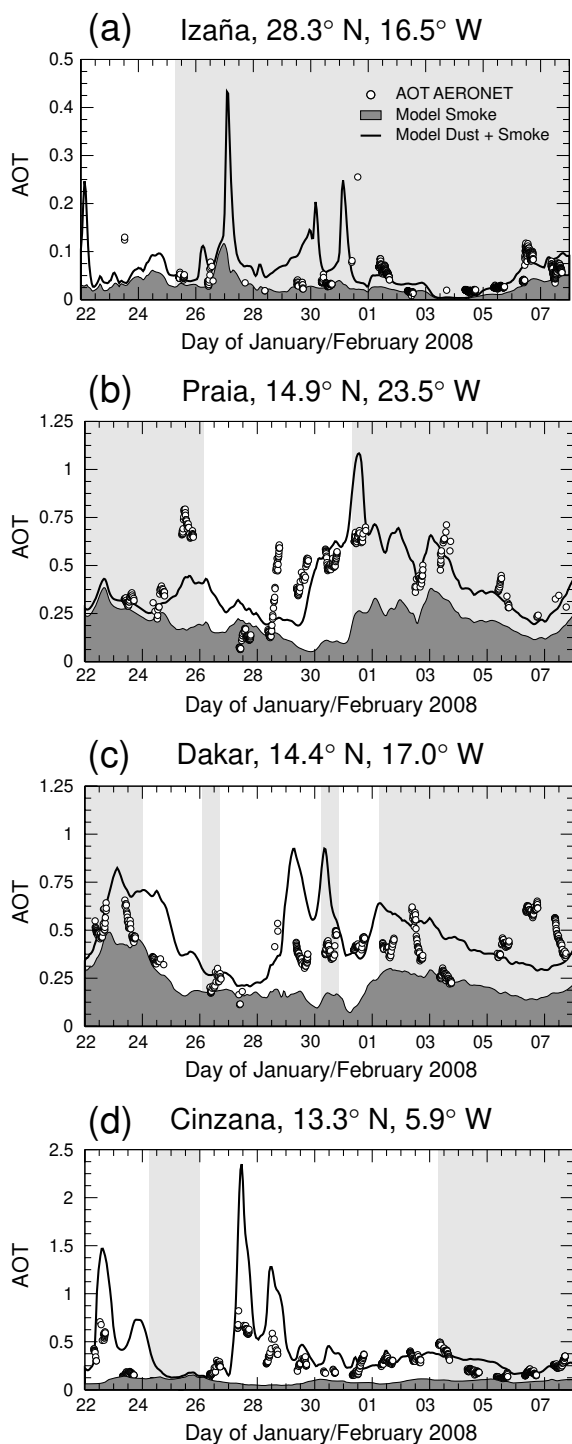
(a) Izaña, 28.3° N, 16.5° W

(b) Praia, 14.9° N, 23.5° W

(c) Dakar, 14.4° N, 17.0° W

(d) Cinzana, 13.3° N, 5.9° W

Fig. 7. Aerosol optical thickness (440 nm) at Izaña/Tenerife, Praia/Santiago, Dakar and Cinzana on 22 January–7 February 2008. Compared are sun photometer measurements provided by AERONET (black circles) and values of optical thickness of modelled smoke (dark grey shaded area) and the mixed plume of dust and smoke (solid black line). Grey shaded areas denote the days, on which the Ångström exponent (å) from AERONET measurements indicates a smoke-dominated aerosol layer (å > 0.3).

likely caused by smoke transport along the West African coast, is not matched by COSMO-MUSCAT (see Fig. 6).

3.2.2. Vertical structure. During SAMUM-2 the Saharan dust layers over Cape Verde varied in intensity and vertical structure on daily basis. Mineral dust dominated the lowest 1.5 km of the atmosphere during intense dust events, but was also frequently mixed with the smoke plume. Layers of smoke were mainly present between 1 and 5 km height. The westerlies south of the subtropical jet caused clean aerosol conditions above 5 km (Knippertz et al., 2011).

The model capability to reproduce the vertical aerosol layering over the Cape Verdes is evaluated against lidar measurements taken during SAMUM-2 at Praia in Fig. 8. For 25 and 31 January, and 6 February the model results are compared to vertical profiles of backscatter coefficients from the BERTHA lidar and for 28 January to extinction coefficients measured by the PO-LIS lidar. Following Tesche et al. (2009) the backscatter coefficients are shown separately for dust, smoke and total aerosol. On 25 January the observed total backscatter coefficient over Praia was about 4–5 Mm^{-1} sr^{-1} in the lowest 1 km agl, and a second maximum of 4 Mm^{-1} sr^{-1} was found in the smoke-dominated layer at about 2 km height (Figs 8a and b). The model matches the dust profile very well, even though the backscatter coefficient is slightly too low within the lowest 1 km. The backscatter coefficient of smoke particles is underestimated by a factor of 4 leading to an underestimation of the total aerosol backscatter around 2 km height. The modelled maximum of the smoke particle backscatter coefficient is located at 2.5 km height. A backward-trajectory analysis reveals, that the air masses arriving at Praia in 2 km originate from fires in Senegal and southwestern Mali (Fig. 7b in Knippertz et al., 2011). The model simulates a significant dust but only a weak smoke transport from these regions as shown by the AOT maps in Figs 6a and e. Therefore, the underestimation of modelled smoke particle backscatter coefficients results from too low vegetation-fire emissions prescribed in the model. For this day observations are also available from the DLR HSRL lidar aboard the Falcon aircraft. Figure 9 depicts an east–west transect of the aerosol extinction coefficient showing layers of Saharan dust and biomass-burning aerosol across Santiago Island in the afternoon on 25 January. The high values near the surface are most likely due to sea salt particles, which were often present during the campaign, but are not considered in the simulations. Again, the observations indicate an underestimation of the modelled smoke extinction coefficient at heights around 2 km. In accordance with the lidar profiling, the dust and smoke transport is computed mainly below 4–4.5 km. However, the aerosol concentration does not decrease to zero at higher levels since the model is too diffusive in vertical transport. The comparison to the aircraft measurements shows that both the agreements and the discrepancies in the modelled vertical aerosol structure are systematic but not only valid for Praia.

During the strong dust event on 28 January extinction coefficients of up to 1 km^{-1} were measured in the lowest 1 km (Fig. 8c).
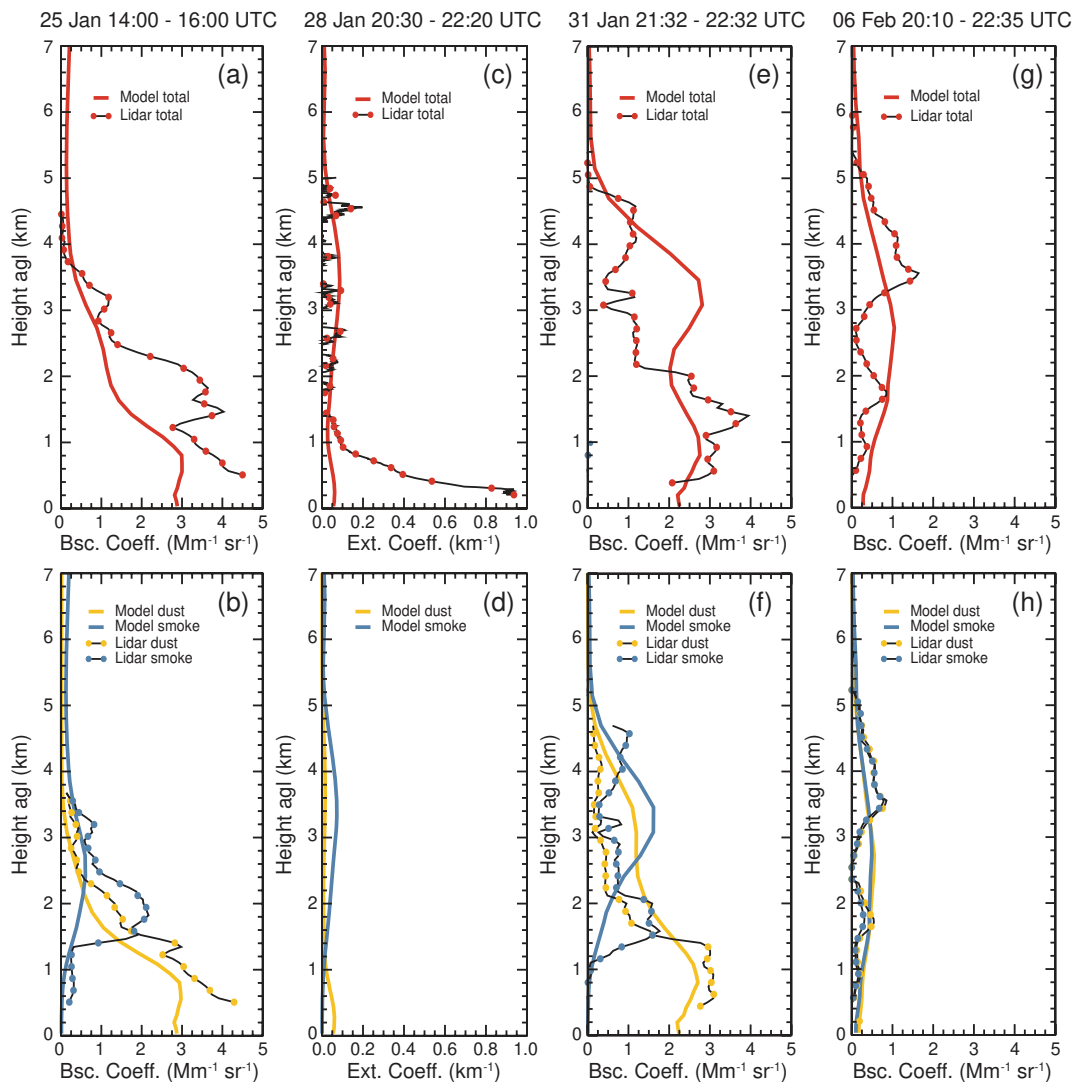
Fig. 8. Vertical profiles of the dust and smoke particle backscatter coefficient (532 nm) at Praia site on 25 January (14:00–16:00 UTC), 31 January (21:32–22:32 UTC) and 6 February (20:10–22:35 UTC) 2008. On 28 January (20:30–22:20 UTC), profiles of extinction coefficients (355 nm) are shown instead. Upper panels: total particle backscatter and extinction coefficients. Lower panels: separate profiles for dust and smoke particles (not available on 28 January). The lidar data (black lines with coloured circles) are compared with modelled profiles (solid coloured lines).

While the model reproduces the reduction in vegetation-fire smoke, which is also indicated by the Ångström exponent, the maximum dust extinction coefficient is dramatically underestimated by the model (Figs 8c and d). This is due to the fact that the responsible dust storm is largely missed as already shown in comparisons with satellite retrievals and sun photometer measurements (cf. Figs 6b and 7b).

On 31 January the model reproduces the magnitude of the dust backscatter coefficient profile except the strong decrease at the top of the dust layer. In the model, dust mixes too efficiently to heights of about 5 km agl, probably caused by the inability of the COSMO to describe the boundary-layer capping inversion or by an overprediction of vertical dust transport over the African

continent. The observations show a maximum of the dust and smoke particle concentration at 1.5 km agl, with a maximum total backscatter coefficient of about 4 Mm^{-1} sr^{-1}. The model simulates a pronounced maximum of biomass-burning aerosol at 3.5 km height, which is not confirmed by the lidar profiles. Consequently, the total backscatter coefficient is overestimated at heights between 2 and 4.5 km (Figs 8e and f).

An overall very good agreement between model results and lidar data is found on 6 February. The modelled backscatter coefficient with values up to 1 Mm^{-1} sr^{-1} is within the range of the measurements. In addition, the simulations reproduce the ratio of desert dust to biomass-burning aerosol and the general reduction in the aerosol load compared to previous days. Still, the
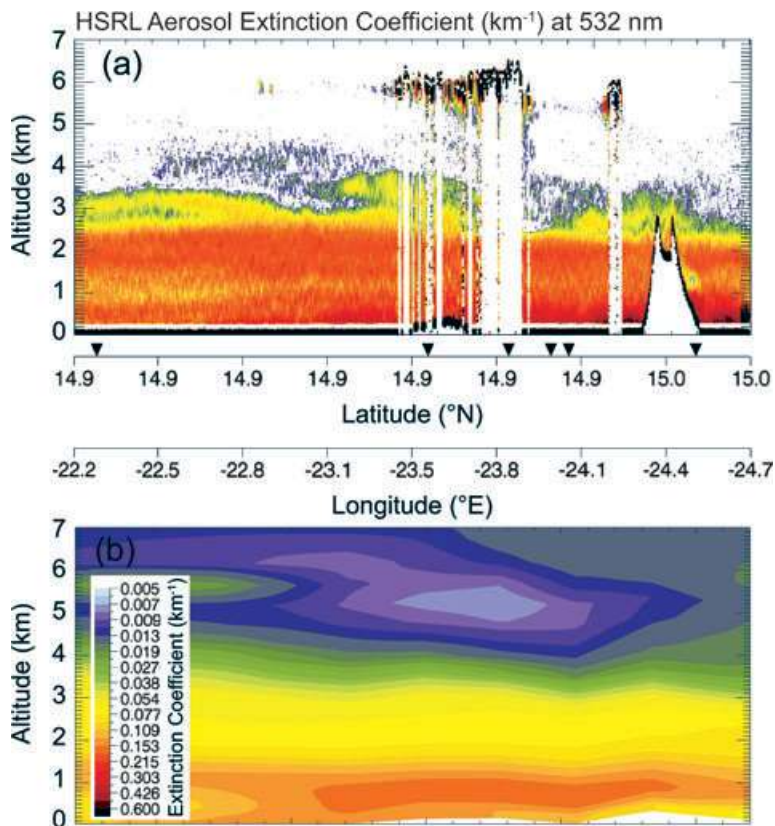
Fig. 9. East–west transect of aerosol extinction coefficient showing the vertical distribution of Saharan dust and biomass-burning aerosol during the Falcon flight across Santiago Island on 25 January 2008 (15:05–15:38 UTC): (a) lidar data from flight measurements and (b) model-derived extinction coefficient. Arrows on the Longitude/Latitude axis indicate changes in the flight direction of the aircraft. The colour bar and axis labels refer to both cross sections.

observed vertical structure is more complex, and single aerosol layers are not resolved by the model (see Figs 8g and h).

3.2.3. Dust particle size distribution. Due to the overlap effect, lidar profiling does not provide trustworthy extinction or backscatter coefficients at the surface. Here, ground-based measurements of the particle size distribution can serve as an additional indicator as to whether the dust production and transport processes are correctly simulated by the model. However, the comparison has to be done carefully since the measured size distributions are affected by local soil dust emissions and sea-salt aerosol present during most of the campaign (Knippertz et al., 2011; Kandler et al., 2011a,b; Schladitz et al., 2011).

For 25 January, near-surface dust number size distribution from model results agree well with ground measurements from a combined DMPS and APS at the Praia site (Fig. 10a). Mineral dust particles are generally found in the size range larger than 0.1 μm diameter (e.g. Schütz et al., 1981). The high number of particles smaller than 0.1 μm in the measurements is not related to dust concentrations. The high number concentration of particles larger than 15 μm indicates locally emitted aerosol particles (Kandler et al., 2011b). Dust particles larger than 10 μm have mostly been removed by mainly dry deposition during long-range transport towards the Cape Verde Islands.

Large discrepancies between modelled dust particle numbers and ground-based size measurements are only found for the dust

outbreak on 28 January (Fig. 10b). The strong mismatch is an indicator for the misrepresentation of the dust outbreak across the tropical Atlantic Ocean in the model results. The underestimation of particle numbers is consistent with the discrepancies in dust optical thickness and extinction coefficient profiles. On 31 January the agreement in dust particle number size distribution between model and surface observations at Praia is reasonable. The modelled dust concentrations of particle diameter sizes around 1 μm is somewhat too high (Fig. 10c), which agrees with the overestimation of the dust AOT in Fig. 7b. The model results reproduce the measurements very well on 6 February, when the dust optical thickness and profiles are modelled realistically (Fig. 10c). In general, the agreement between model-derived dust particle number size distributions and ground-based size observations is best when the spatio-temporal dust distribution is also modelled correctly (based on comparisons of optical thickness and backscatter/extinction coefficients). In turn, reliable size distributions are needed to compute dust optical quantities for model validation.

4. Conclusions

The regional model-system COSMO-MUSCAT was applied to simulate the spatial and temporal evolution of the mixed plume of Saharan dust and biomass-burning aerosol for the period of
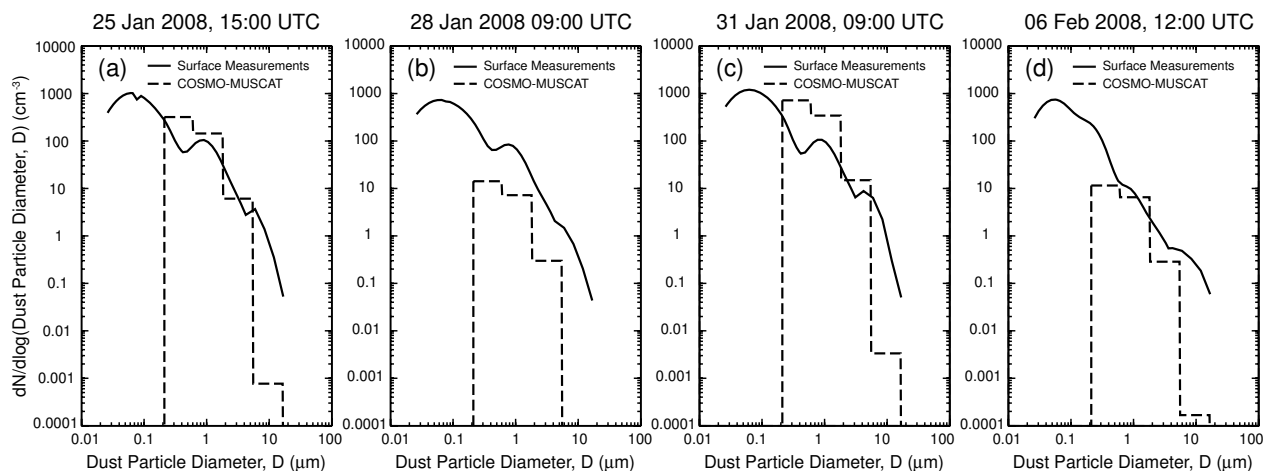
Fig. 10. Ground-level number size distribution at the SAMUM-2 site Praia on 25 (15:00 UTC), 28 (09:00 UTC) and 31 January (09:00 UTC) and 6 February (12:00 UTC) 2008. Model results for the first layer at about 34 m height (dashed line), measurements from a combined DMPS/APS system at about 5 m height (solid line). Note, the observation data are truncated at 20 μm to exclude locally emitted large particles.

the second SAMUM field experiment in January and February 2008. Standard ground-based, airborne and space-borne remote sensing, and in situ measurements from the field campaign were used for a detailed model evaluation. A particular focus was on the days 25, 28 and 31 January, and 6 February which are representative for characteristic transport scenarios. Moreover, data of many colocated airborne and ground-based measurements are available for these days.

Comparisons with maps of DSAs derived from the MSG infrared dust index and observations at several weather stations show that the model is able to reproduce the widespread uplift of mineral dust from Mauritania to the Bodélé Depression in most cases. Even though the dry synoptic-scale dynamics that cause dust events during the winter season are well matched by the meteorological model, surface winds and dust distributions are not always satisfactorily reproduced. So, the model mostly fails to simulate the pure dust case on 28 January, which is underestimated. The dust emissions in this case were associated with the breakdown of nocturnal LLJs. The COSMO model simulates the LLJ formation over the Sahara and the Sahelian region, but the typical peak in surface wind speeds during the morning hours caused by the degradation of LLJs is often not reproduced or underestimated. The reason is that the downward mixing of momentum occurs too gradually in the model. Possibly, the discrepancies are due to shortcomings of the turbulence parametrization. As a result West African dust emissions are too low and possibly delayed, and subsequent dust transport across the tropical Atlantic Ocean is misrepresented.

The representation of the mineral dust plume is expectedly complicated, as strength and location of dust sources are interactively based on modelled surface winds. Nevertheless, considerable uncertainties also exist in the vegetation-fire emissions that are prescribed using satellite observations. The uncertainties are mainly caused by clouds and spatial errors affecting

the satellite fire detection products used to compute the smoke. In particular, West African fires situated in the vicinity of the ITCZ are frequently obscured by clouds. In addition, the fire emission parameters available from literature are averages over large numbers of fires with different combustion states that do not necessarily represent the characteristics of individual land fires. Systematic gaps in MODIS fire maps from day to day may not affect climate model runs, but are problematic for regional biomass-burning modelling. Vegetation-fire emissions are simulated in a broad belt across West Africa as prescribed on the basis of MODIS fire location data. The fire emissions appear to be overestimated along the coast from Guinea to Cote d'Ivoire. In contrast, over the western Gulf of Guinea the modelled particle optical depth is often lower than observations as the fire maps used for model initialization are contaminated by clouds. In addition, industrial and urban pollution along the Gulf of Guinea coast, which is not accounted for by the fire location data set might contribute to the high load of absorbing aerosol in this region. However, it is also possible that the simulated Bodélé dust emissions are too low.

Accordingly, the modelled transport patterns of Saharan dust and biomass-burning smoke agree reasonably well with satellite retrievals. Also, the model-derived optical thickness of dust and smoke are mostly in agreement with the sun photometer measurements. In general, the ratio of model-predicted dust to smoke aerosol follows the temporal evolution of the observed Ångström exponent that indicates whether dust or smoke dominates the aerosol layer.

Comparisons with lidar measurements at the Praia site show that the model captures the principle features of the observed aerosol layering of dust and biomass-burning aerosol, which is an important pre-requisite for studies on the radiative aerosol effects and their impacts on atmospheric dynamics and transport. Transport of Saharan dust towards the Cape Verde Islands is

simulated mainly below 1–1.5 km height. Except the pure dust event on 28 January, there is also a good agreement between the simulated dust size distribution and ground measurements of aerosol particle size. The computed smoke plume from the tropical West Africa reaches the Cape Verdes above 1–2 km height.

The simulations demonstrate the limits in regional modelling the complex aerosol plume composed of mineral dust and biomass-burning smoke transported off the West African continent during the dry season. Therefore, further efforts are needed to improve our understanding of relevant meteorological processes forcing Saharan dust emissions and to find ways of better representing them in regional and global dust models. With respect to vegetation-fire smoke, satellite-based measures of fire radiative energy have been shown to be an effective alternative for estimating biomass-burning emissions. In addition, a combination of observations from several satellite instruments could overcome some of the described difficulties.

However, the regional model system reproduces the general features of the mixed dust and smoke aerosol distribution during the SAMUM-2 field campaign. Transport patterns, AOTs and the vertical structure of aerosol layers mainly agree with the observations. The model results are a useful basis for follow-up studies on the direct radiative effects and feedbacks of mixtures of Saharan dust and biomass-burning aerosol using COSMO-MUSCAT.

5. Acknowledgments

References

Althausen, D., Müller, D., Ansmann, A., Wandinger, U., Hube, H. and co-authors. 2000. Scanning 6-wavelength 11-channel aerosol lidar. *J. Atmos. Oceanic Technol.* **17**, 1469–1482.

Andreae, M. O. and Merlet, P. 2001. Emission of trace gases and aerosols from biomass burning. *Global Biogeochem. Cycles* **15**, 955–966.

Ansmann, A., Petzold, A., Kandler, K., Tegen, I., Wendisch, M. and co-authors. 2011. Saharan Mineral Dust Experiments SAMUM–1 and SAMUM–2: what have we learned? *Tellus* **63B**, this issue.

Barbosa, P. M., Stroppiana, D., Gregoire, J. M. and Pereira, J. M. C. 1999. An assessment of vegetation fire in Africa (1981–1991): burned areas, burned biomass, and atmospheric emissions. *Glob. Biogeochem. Cycle* **13**, 933–950.

Berge, E. 1997. Transboundary air pollution in Europe. In: *MSC-W Status Report 1997, Part 1 and 2, EMEP/MSC-W Report 1/97*, The Norwegian Meteorological Institute, Oslo.

Brown, S. and Gaston, G. 1996. Estimates of biomass density for tropical forests. In: *Biomass Burning and Global Change. Remote Sensing, Modeling and Inventory Development, and Biomass Burning in Africa*, Volume 1 (ed. Levine, J. S.). MIT Press, Cambridge, MA, 133–139.

D'Almeida, G. A. 1986. A model for Saharan dust transport. *J. Clim. Appl. Meteorol.* **25**, 903–916.

Esselborn, M., Wirth, M., Fix, A., Weinzierl, B., Rasp, K. and co-authors. 2009. Spatial distribution and optical properties of Saharan dust observed by airborne high spectral resolution lidar during SAMUM 2006. *Tellus* **61B**, doi:10.1111/j.1600-0889.2008.00394.x.

Friedl, M. A., McIver, D. K., Hodges, J. C. F., Zhang, X. Y., Muchoney, D. and co-authors. 2002. Global land cover mapping from MODIS: algorithms and early results. *Int. J. Remote Sens.* **83**, 287–302.

Gibbs, H. K., Brown, S., Niles, J. O. and Foley, J. A. 2007. Monitoring and estimating tropical forest carbon stocks: making REDD a reality. *Environ. Res. Lett.* **4**, 045023, doi:10.1088/1748-9326/2/4/045023.

Groß, S., Tesche, M., Freudenthaler, V., Toledano, C., Wiegner, M. and co-authors. 2011. Characterization of Saharan dust, marine aerosols and mixtures of biomass burning aerosols and dust by means of multi-wavelength depolarization and Raman measurements during SAMUM 2. *Tellus* **63B**, this issue.

Haywood, J. M., Pelon, J., Formenti, P., Bharmal, N., Brooks, M. and co-authors. 2008. Overview of the dust and biomass-burning experiment and African monsoon multidisciplinary analysis special observing period-0. *J. Geophys. Res.* **113**, doi:10.1029/2008JD010077.

Heinold, B., Helmert, J., Hellmuth, O., Wolke, R., Ansmann, A. and co-authors. 2007. Regional modeling of Saharan dust events using LM-MUSCAT: model description and case studies. *J. Geophys. Res.* **112**, D11204, doi:10.1029/2006JD007443.

Heinold, B., Tegen, I., Schepanski, K. and Hellmuth, O. 2008. Dust radiative feedback on Saharan boundary layer dynamics and dust mobilization. *Geophys. Res. Lett.* **35**, L20817, doi:10.1029/2008GL035319.

Heinold, B., Tegen, I., Esselborn, M., Kandler, K., Knippertz, P. and co-authors. 2009. Regional Saharan dust modelling during the SAMUM 2006 campaign. *Tellus* **61B**, doi:10.1111/j.1600-0889.2008.00387.x.

Heinold, B., Tegen, I., Bauer, S. and Wendisch, M. 2011. Regional modelling of Saharan dust and biomass burning smoke, part 2: direct radiative forcing and atmospheric dynamic response. *Tellus* **63B**, this issue.

Heintzenberg, J. 2009. The SAMUM–1 experiment over Southern Morocco: overview and introduction. *Tellus* **61B**, doi:j.1600-0889.2008.00403.x.

Helmert, J., Heinold, B., Tegen, I., Hellmuth, O. and Wendisch, M. 2007. On the direct and semi-direct effect of Saharan dust over Europe: a modeling study. *J. Geophys. Res.* **112**, D11204, doi:10.1029/2006JD007444.

Heese, B., Freudenthaler, V., Seefeldner, M. and Wiegner, M. 2002. POLIS: a new portable system ground-based and airborne measurements of aerosols and clouds. In: *Lidar Remote Sensing in Atmospheric and Earth Science*, (eds. L. R., Bissonnette, G., Roy and G., Vallee) Defence Research and Development, Canada-Valcartier, Val-Belair, QU, Canada, 71–74.

Holben, B. N., Eck, T. F., Slutsker, I., Tanre, D., Buis, J. P. and co-authors. 1998. AERONET: a federated instrument network and data archive for aerosol characterisation. *Remote Sens. Environ.* **66**, 1–16.

Hyer, E. J. and Reid, J. S. 2009. Baseline uncertainties in biomass burning emission models resulting from spatial error in satellite active fire location data. *Geophys. Res. Lett.* **36**, L05802, doi:10.1029/2008GL036767.

IPCC 2007. Climate change 2007: the physical science basis. Contribution of Working Group I to the Forth Assessment Report of the Intergovernmental Panel on Climate Change, (eds. S. Solomon, D. Quin, M. Manning, Z. Chen, M. Marquis, K. B. Averyt, M. Tignor and H. L. Miller), Cambridge University Press, New York.

Jakobson, H. A., Jonson, J. E. and Berge, E. 1997. The multi-layer Eulerian model: model description and evaluation of transboundary fluxes of sulphur and nitrogen species for one year. EMEP/MSC-W Note 2/97, The Norwegian Meteorological Institute, Oslo, Norway.

Justice, C. O., Giglio, L., Korontzi, S., Owens, J., Morissette, J. T. and co-authors. 2002. The MODIS fire products. *Remote. Sens. Environ.* **83**, 244–262.

Kandler, K., Lieke, K., Benker, N., Küpper, M., Emmel, C. and co-authors. 2011a. Ground-based off-line aerosol measurements at Praia, Cape Verde, during the Saharan Mineral Dust Experiment: microphysical properties and mineralogy. *Tellus* **63B**, this issue.

Kandler, K., Schütz, L., Jäckel, S., Lieke, K., Emmel, C. and co-authors. 2011b. Electron microscopy of particles collected at Praia, Cape Verde, during the Saharan Mineral dust experiment: particle chemistry, shape, mixing state and complex refractive index. *Tellus* **63B**, this issue.

Knippertz, P., Tesche, M., Heinold, B., Kandler, K., Schladitz, A. and co-authors. 2011. Dust mobilization and transport from West Africa to Cape Verde: a meteorological overview of SAMUM–2. *Tellus* **63B**, this issue.

Knoth, O. and Wolke, R. 1998. Implicit-explicit Runge-Kutta methods for computing atmospheric reactive flow. *Appl. Num. Math.* **28**, 327–341.

Laurent, B., Marticorena, B., Bergametti, G., Leon, J. F. and Mahowald, N. M. 2008. Modeling mineral dust emissions from the Sahara desert using new surface properties and soil database. *J. Geophys. Res.* **113**, D14218, doi:10.1029/2007JD009484.

Laurent, B., Tegen, I., Heinold, B., Schepanski, K., Weinzierl, B. and co-authors. 2010. A model study of Saharan dust emissions and distributions during SAMUM-1 campaign. *J. Geophys. Res.* **115**, D21210, doi:10.1029/2009JD012995.

Levelt, R. F. 2002. OMI algorithm theoretical basis document volume 1: OMI instrument, level 0-1b processor, calibration & operations. Technical Report, NASA Goddard Space Flight Center, Greenbelt, MD.

Majewski, D., Liermann, D., Prohl, P., Ritter, B., Buchhold, M. and co-authors. 2002. The operational global icosahedral-hexagonal grid-point model GME: description and high-resolution tests. *Mon. Wea. Rev.* **130**, 319–338.

Marticorena, B. and Bergametti, G. 1995., Modeling the atmospheric dust cycle: 1. Design of a soil-derived dust emission scheme. *J. Geophys. Res.* **100**, 16 415–16 430.

Miller, R. L., Perlwitz, J. and Tegen, I. 2004. Feedback upon dust emission by dust radiative forcing through the planetary boundary layer. *J. Geophys. Res.* **109**, D24209, doi:10.1029/2004JD004912.

Moody, E. G., King, M. D., Platnick, S., Schaaf, C. B. and Gao, F. 2005., Spatially complete global spectral surface albedos: value-added datasets derived from terra MODIS land products. *IEEE Trans. Geosci. Remote Sensing* **43**, 144–158.

Myhre, G., Grini, A., Haywood, J. M., Stordal, F., Chatenet, B. and co-authors. 2003. Modeling the radiative impact of mineral dust during the Saharan Dust Experiment (SHADE) campaign. *J. Geophys. Res.* **108**(D18), 8579, doi:10.1029/2002JD002566.

Myhre, G., Hoyle, C. R., Berglen, T. F., Johnson, B. T. and Haywood, J. M. 2008. Modeling of the solar radiative impact of biomass burning aerosols during the Dust and Biomass-burning Experiment (DABEX). *J. Geophys. Res.* **113**, D00C16, doi:10.1029/2008JD009857.

Reid, J. S., Koppmann, R., Eck, T. F. and Eleuterio, D. P. 2005a. A review of biomass burning emissions part II: intensive physical properties of biomass burning particles. *Atmos. Chem. Phys.* **5**, 799–825.

Reid, J. S., Eck, T. F., Christopher, S. A., Koppmann, R., Dubovik, O. and co-authors. 2005b. A review of biomass burning emissions part III: intensive optical properties of biomass burning particles. *Atmos. Chem. Phys.* **5**, 827–849.

Renner, E. and Wolke, R. 2010. Modelling the formation and atmospheric transport of secondary inorganic aerosols with special attention to regions with high ammonia emissions. *Atmos. Environ.* **44**, 1904–1912.

Running, S. W., Thornton, P. E., Nemani, R. and Glassy, J. M. 2000. Global terrestrial gross and net primary productivity from the Earth Observing System. In: *Methods in Ecosystem Science* (eds. Sala, O., Jackson, R. and Mooney, H.). Springer Verlag, New York, 44–57.

Schepanski, K., Tegen, I., Laurent, B., Heinold, B. and Macke, A. 2007. A new Saharan dust source activation frequency map derived from MSG-SEVIRI IR-channels. *Geophys. Res. Lett.* **34**, L18803, doi:10.1029/2007GL030168.

Schepanski, K., Tegen, I., Todd, M. C., Heinold, B., Bönisch, G. and co-authors. 2009. Meteorological processes forcing Saharan dust emission inferred from MSG-SEVIRI observations of subdaily dust source activation and numerical models. *J. Geophys. Res.* **114**, D10201, doi:10.1029/2008JD010325.

Schladitz, A., Müller, T., Nowak, A., Kandler, K., Lieke, K. and co-authors. 2011. In situ aerosol characterization at Cape Verde. Part 1: particle number size distributions, growth factors and hygroscopic mixing state of mixed marine and Saharan dust aerosol. *Tellus* **63B**, this issue.

Schütz, L., Jaenicke, R. and Pietrek, H. 1981. Saharan dust transport over the North Atlantic Ocean. *Geol. Soc. Am. Special Paper* **186**, 87–100.

Seiler, W. and Crutzen, P. J. 1980. Estimates of gross and net fluxes of carbon between the biosphere and atmosphere from biomass burning. *Clim. Change* **2**, 207–247.

Seinfeld, J. H. and Pandis, S. N. 1998. *Atmosheric Chemistry and Physics*, pp. 1326, John Wiley & Sons, New York.

Simpson, J., Kummerow, C., Tao, W. K. and Adler, R. F. 1996. On the tropical rainfall measuring mission (TRMM). *Meteorol. Atmos. Phys.* **60**, 19–36.

Sofiev, M., Vankevich, R., Lotjonen, M., Prank, M., Petukhov, V. and co-authors. 2009. An operational system for the assimilation of the satellite information on wild-land fires for the needs of air quality modelling and forecasting. *Atmos. Chem. Phys.* **9**, 6833–6847.

Solmon, F., Mallet, M., Elguindi, N., Giorgi, F., Zakey, I. and co-authors. 2008. Dust impact on Sahelian precipitation gradients, mechanisms and sensitivity to absorption properties. *J. Geophys. Res.* **35**, L24705, doi:10.1029/2008GL035900.

Sokolik, I. N. and Toon, O. B. 1996. Direct radiative forcing by anthropogenic airborne mineral aerosols. *Nature* **381**, 681–683.

Sokolik, I. N. and Toon, O. B. 1999. Incorporation of mineralogical composition into models of the radiative properties of mineral aerosol from UV to IR wavelengths. *J. Geophys. Res.* **104**, 9423–9444.

Steppeler, J., Doms, G. Schättler, U., Bitzer, H. W., Gassmann, A. and co-authors. 2003. Meso-gamma scale forecasts using the non-hydrostatic model LM. *Meteorol. Atmos. Phys.* **107**(D21), 4576, doi:10.1007/s00703-001-0592-9, 75–96.

Tegen, I., Harrison, S. P., Kohfeld, K., Prentice, I. C., Coe, M. and Heimann, M. 2002. Impact of vegetation and preferential source areas on global dust aerosol: results from a model study. *J. Geophys. Res.* **107**(D21), 4576, doi:10.1029/2001JD000963.

Tegen, I., Heinold, B., Todd, M., Helmert, J., Washington, R. and co-authors. 2006. Modelling soil dust aerosol in the Bodélé depression during the BoDEx campaign. *Atmos. Chem. Phys.* **6**, 4171–4211.

Tegen, I., Bierwirth, E., Heinold, B., Helmert, J. and Wendisch, M. 2010. Effect of measured surface albedo on modeled Saharan dust solar radiative forcing. *J. Geophys. Res.* **115**, D24312, doi:10.1029/2009JD013764.

Tesche, M., Ansmann, A., Müller, D., Althausen, D., Engelmann, R. and co-authors. 2009. Vertically resolved separation of dust and smoke over Cape Verde by using multiwavelength Raman and polarization lidars during Saharan Mineral Dust Experiment 2008. *J. Geophys. Res.* **114**, doi:10.1029/2009JD011862.

Tesche, M., Ansmann, A., Müller, D., Althausen, D., Mattis, I. and co-authors. 2011. Profiling of Saharan dust and biomass burning smoke with multiwavelength polarization Raman lidar at Cape Verde. *Tellus* **63B**, this issue.

Thornton, P. E., Law, B. E., Gholz, H. L., Clark, K. L., Falge, E. and co-authors. 2006. Modeling and measuring the effects of disturbance history and climate on carbon and water budgets in evergreen needle-leaf forests. *Agric. For. Meteorol.* **113**, 185–222.

Tiedtke, M. 1989. A comprehensive mass flux scheme for cumulus parameterisation in large-scale models.. *Mon. Wea. Rev.* **117**, 1779–1799.

Todd, M. C., Washington, R., Raghavan, S., Lizcano, G. and Knippertz, P. 2008. Regional model simulations of the Bodélé low-level jet of northern Chad during the Bodélé Dust Experiment (BoDEx 2005). *J. Clim.* **21**, 995–1012.

Toledano, C., Wiegner, M., Garhammer, M., Seefeldner, M., Garsteiger, J. and co-authors. 2011. Sun photometer observations during SAMUM 2008: retrieval of spectral particle optical depth, Ångström exponents, and microphysical properties. *Tellus* **63B**, this issue.

Tsyro, S. and Erdman, L. 2000. Parameterization of aerosol deposition processes in EMEP MSC-E and MSC-W transport models. In: *EMEP/MSC-W Note 7/00*, The Norwegian Meteorological Institute, Oslo.

van der Werf, G. R., Randerson, J. T., Giglio, L., Collatz, G. J., Kasibhatla, P. S. and co-authors. 2006. Interannual variability in global biomass burning emissions from 1997 to 2004. *Atmos. Chem. Phys.* **6**, 3423–3441.

van der Werf, G. R., Randerson, J. T., Giglio, L., Collatz, G. J., Mu, M. and co-authors. 2010. Global fire emissions and the contribution of deforestation, savanna, forest, agricultural, and peat fires (1997-2009). *Atmos. Chem. Phys.* **10**, 11 707–11 735, doi:10.5194/acp-10-11707-2010.

Washington, R., Todd, M. C., Middleton, N. J. and Goudie, A. S. 2003. Dust-storm source areas determined by the Total Ozone Monitoring Spectrometer and surface observations. *Ann. Assoc. Am. Geogr.* **93**, 297–313.

Wolke, R. and Knoth, O. 2000. Implicit-explicit Runge-Kutta methods applied to atmospheric chemistry-transport modelling. *Environ. Model. Softw.* **15**, 711–719.

Wolke, R., Hellmuth, O., Knoth, O., Schröder, W., Heinrich, B. and co-authors. 2004. The chemistry-transport modeling system LM-MUSCAT: description and CityDelta applications in: *Air Pollution Modeling and Its Application XVI*, (eds. C. Borrego and S. Incecik), *in Proceedings of Twenty-sixth NATO/CCMS International Technical Meeting on Air Pollution Modeling and its Application*, Kluver Academic/Plenum Publishers, New York.

Yoshioka, M., Mahowald, N., Conley, A. J., Collins, W. D., Fillmore, D. W. and co-authors. 2007. Impact of desert dust radiative forcing on Sahel precipitation: relative importance of dust compared to sea surface temperature variations, vegetation changes, and greenhouse gas warming. *J. Clim.* **20**, 1445–1467.

Zender, C., Newman, D. S. and Torres O. 2003. Spatial heterogeneity in aeolian erodibility: uniform, topographic, geomorphic, and hydrologic hypotheses. *J. Geophys. Res.* **108**(D17), 4543, doi:10.1029/2002JD003039.

Zhang, L., Gong, S., Padro, J. and Barrie, L. 2001. A size-segregated particle dry deposition scheme for an atmospheric aerosol module. *Atmos. Environ.* **35**, 549–560.